Mon. Not. R. Astron. Soc. **000**, 1–5 (2016) Printed 28 March 2016 (MN LATEX style file v2.2)

# Evidence that widespread star formation may be underway in G0.253+0.016, "The Brick"

K. A. Marsh[1⋆], S. E. Ragan[2], A. P. Whitworth[1], & P. C. Clark[1]
[1] *School of Physics and Astronomy, Cardiff University, Cardiff CF24 3AA, UK*
[2] *School of Physics and Astronomy, The University of Leeds, Leeds, LS2 9JT, UK*

28 March 2016

**ABSTRACT**
Image cubes of differential column density as a function of dust temperature are constructed for Galactic Centre molecular cloud G0.253+0.016 ("The Brick") using the recently described PPMAP procedure. The input data consist of continuum images from the *Herschel* Space Telescope in the wavelength range 70–500 $\mu$m, supplemented by previously published interferometric data at 1.3 mm wavelength. While the bulk of the dust in the molecular cloud is consistent with being heated externally by the local interstellar radiation field, our image cube shows the presence, near one edge of the cloud, of a filamentary structure whose temperature profile suggests internal heating. The structure appears as a cool ($\sim$ 14 K) tadpole-like feature, $\sim$ 6 pc in length, in which is embedded a thin spine of much hotter ($\sim$ 40–50 K) material. We interpret these findings in terms of a cool filament whose hot central region is undergoing gravitational collapse and fragmentation to form a line of protostars. If confirmed, this would represent the first evidence of widespread star formation having started within this cloud.

**Key words:** Galaxy: centre — ISM: clouds — submillimetre: ISM — techniques: high angular resolution — stars: formation — stars: protostars.

## 1 INTRODUCTION

The dense molecular cloud, G0.253+0.016 (also known as "The Brick"), has been the subject of intense recent study as a likely future site of prolific high-mass star formation (Longmore et al. 2012; Rathborne et al. 2014a). However, with the exception of a 22 GHz water maser source (Lis et al. 1994), likely associated with a self gravitating core (Rathborne et al. 2014b), no clear evidence of star formation has been reported to date. More recent observations at centimetre wavelengths (Mills et al. 2015) have not revealed any additional maser activity attributable to star formation. Thus the question remains: what has delayed or is preventing prodigious star formation in the Brick? Dynamical arguments, such as its highly turbulent nature (Kauffmann et al. 2013; Johnston et al. 2014; Rathborne et al. 2015) or its apparent location within a coherent ring-like stream of molecular clouds in orbit about Sgr A$^*$ (Molinari et al. 2011; Longmore et al. 2013; Kruijssen et al. 2015) have been cited as possible agents of star formation suppression. In order to set more stringent constraints on the level of star formation activity, it would seem worthwhile to examine other possible indicators, such as the presence of localised peaks in dust temperature that might signal the presence of protostars at early stages of evolution. With this in mind, we present here the results of a detailed study of the variation of dust temperature within the cloud.

Studies of the temperature structure of the Brick show that the gas temperature is uniformly higher than the dust temperature and that those two components are heated by different mechanisms. The observed dust temperatures of $T_{\rm D} \sim$ 19–27 K (Longmore et al. 2012) are consistent with heating by the local interstellar radiation field (ISRF) assuming that the latter is $\sim$ 1000 times stronger than that in the solar vicinity (Clark et al. 2013). However, the gas (Güsten et al. 1981; Mills & Morris 2013, $T_{\rm G} \sim$ 60–100 K) is most likely heated by a combination of cosmic rays (Clark et al. 2013) and turbulent compression (Ginsburg et al. 2016), with the former dominating at high densities.

Our study of the dust temperature distribution makes use of the PPMAP procedure (Marsh et al. 2015), whose purpose is to generate resolution-enhanced image cubes of differential column density as a function of dust temperature, $T_{\rm D}$, and sky position $(x, y)$, given sets of observed images of dust continuum emission at multiple wavelengths. Differential column density, in this case, is defined as the column density of material (gas plus dust) per unit interval of dust temperature, and is expressed in units of hydrogen

⋆ E-mail: Ken.Marsh@astro.cf.ac.uk

molecules per square centimetre per degree Kelvin. PPMAP is a Bayesian technique whose output is the expectation value of the differential column density in each cell of an image cube whose axes are $(x, y, T_{\rm D})$, given the input data. The *a priori* probability of cell occupancy is controlled by a "dilution" parameter, $\eta$, such that the smaller the value of $\eta$, the more the algorithm tries to fit the data with as few source components as possible. The exact value of $\eta$ is not critical, but the most appropriate value is one which results in a reduced chi squared value of order unity, indicating that the data have been fit within the error bars using a minimum number of source components. The procedure also yields a corresponding image cube of uncertainty values. Errors are Poisson-like, and increase in regions of high total column density. A key underlying assumption is that the dust is optically thin at all wavelengths of observation. PPMAP takes full account of the point spread functions (PSFs) of the telescopes used, and does not require all images to be degraded to the same resolution.

## 2 OBSERVATIONAL DATA AND ANALYSIS PROCEDURE

The principal inputs to PPMAP consist of a set of observed images of dust continuum emission, their associated PSFs, the assumed dust opacity law over the wavelength range of the observations, and a grid of temperature values at which the differential column density will be estimated. The output is then an image cube of differential column density as a function of angular position on the set of predefined temperature planes, plus a corresponding image cube of uncertainty values.

Our observational data consist of a set of *Herschel* PACS and SPIRE images at wavelengths of 70 $\mu$m[1], 160 $\mu$m, 250 $\mu$m, 350 $\mu$m, and 500 $\mu$m, observed as part of the Hi-GAL survey (Molinari et al. 2010). The spatial resolution values of these maps, i.e., the beam sizes at full width half maximum (FWHM), are approximately 8.5″, 13.5″, 18.2″, 24.9″, and 36.3″, respectively. The associated PSFs are based on the measured *Herschel* beam profiles (Poglitsch et al. 2010; Griffin et al. 2013). The adopted temperature grid consists of 12 temperatures equally spaced in $\log T_{\rm D}$ between 7 K and 60 K. These temperatures may be regarded as the approximate midpoints of a set of finite intervals, the $i^{\rm th}$ of which may be expressed as $[(T_{i-1}+T_i)/2, (T_i+T_{i+1})/2]$. The spatial sampling interval of the output grid is 4″ per pixel.

[1] Although the Brick is known to be optically thick ($\tau \sim 1$) at 70 $\mu$m (see, for example, Longmore et al. 2012), we include the 70 $\mu$m image in order to make use of the information it provides on the possible presence of hot material, of particular value when searching for potential sites of star formation. Although this violates a key assumption in PPMAP, the inclusion of a single wavelength for which the source is partially optically thick does not seriously impact the temperature and column density estimates, since those quantities are well constrained by the longer-wavelength data within the optically-thin regime. The benefit is that it facilitates the detection of any hot components whose column densities may be too low for detection at longer wavelengths. Tests with synthetic data confirm these expectations.

Following Rathborne et al. (2015), we adopt the following form for the variation of dust opacity with wavelength:

$$\kappa(\lambda) = 0.042\,{\rm cm^2\,g^{-1}} \left(\frac{\lambda}{300\,\mu{\rm m}}\right)^{-1.2} . \qquad (1)$$

in which the power law index is based on the Rathborne et al. (2015) estimate of $\beta = 1.2 \pm 0.1$, and the coefficient is extrapolated from their 1.2 mm value of 0.8 cm$^2$ g$^{-1}$ based on Ossenkopf & Henning (1994). It is expressed in terms of the total mass (dust plus gas). In comparing the observed fluxes with model values, allowance must be made for the fact the observations represent averages over finite bandpasses rather than monochromatic values. Since the published PACS and SPIRE fluxes are based on an assumed source spectrum which is flat in $\nu F_\nu$, allowance must therefore be made for other spectral shapes. In PPMAP, temperature-dependent colour corrections are applied to the model images using the tables presented by Pezzuto (2013) and Valtchanov (2014).

Fig. 1 shows the results in the form of a set of differential column density images for each of the nine dust temperature planes in which significant column density is detected. We have also produced an image cube of higher spatial resolution by supplementing the *Herschel* data with an interferometric image at 1.3 mm wavelength, published by Johnston et al. (2014), based on observations made with the Submillimeter Array (SMA). In doing so, the SMA image was treated in the same way as for the *Herschel* images, i.e., as a separate input image with its own PSF. The properties of the latter were determined by the interferometer configuration of the SMA whereby the lack of baselines shorter than 16.4 m had the effect of suppressing spatial information on angular scales $\gtrsim 20''$, leading to a zero-sum PSF. Also, since the resolution of the 1.3 mm image ($4.3'' \times 2.7''$) exceeds the Nyquist limit for representation on the 4″ output grid, the 1.3 mm image was smoothed by a Gaussian designed to produce an effective beam FWHM of 8″, and the same smoothing was applied to the PSF. The result is shown in Fig. 1.1 which, due to space limitations, is available in the on-line version of this Letter only.

Although the multi-temperature maps of Figs. 1 and 1.1 look quite similar, detailed examination reveals that the inclusion of the 1.3 mm data has not only increased the spatial resolution, but has also increased the detection significance of the lowest-temperature structures. We base our subsequent discussion on the results obtained using the full six-wavelength data set (*Herschel* plus 1.3 mm), which yield a final spatial resolution of approximately 8″.

Figs. 1 and 1.1 show that at the lowest temperature ($T_{\rm D} = 13.9$ K) the only visible structure is a $\sim 6$ pc tadpole-like feature with a prominent condensation at its head. In the next temperature steps, other features become visible, and at $T_{\rm D} = 26.6$ K the structure is dominated by material around the outside of the cloud—there is a depression in the interior representing a deficit of material at that temperature. The deficit becomes even more pronounced at $T_{\rm D} = 31.3$ K, whereby the interior appears to be devoid of material. Such behaviour is not unexpected for the Brick itself since the material at that temperature is believed to be limited to a thin outer shell (Clark et al. 2013). The apparent limb brightening in the $T_{\rm D} = 31.3$ K panel is consistent with that prediction. However, one would nevertheless ex-

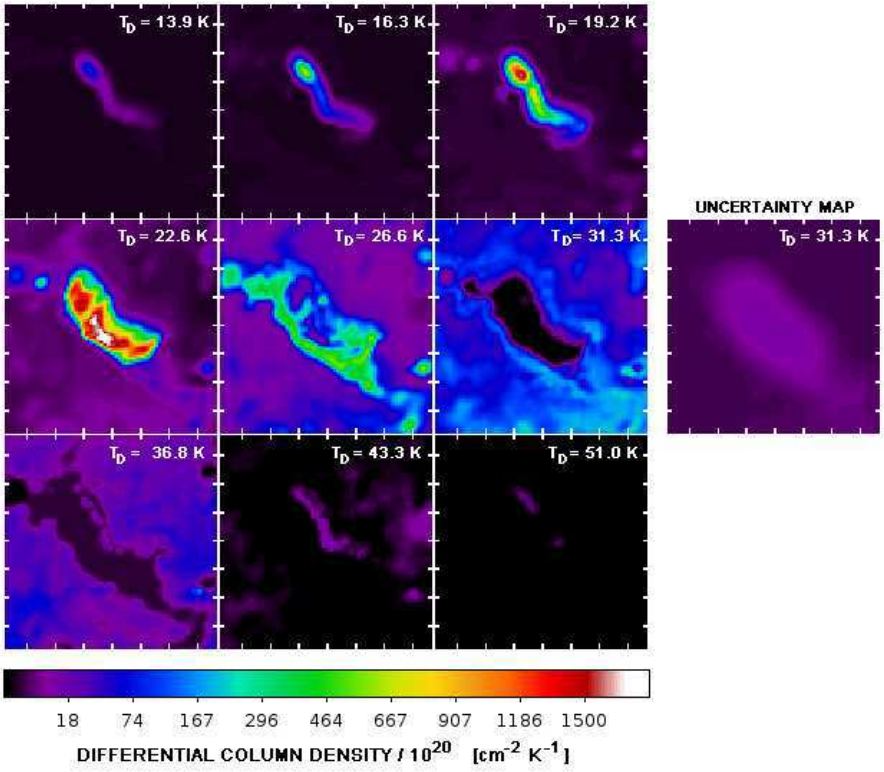


**Figure 1.** Estimated differential column-density of the Brick in nine different planes of dust temperature, $T_{\rm D}$, as indicated in the top right of each panel. The differential column density is expressed in terms of the number density of $H_2$ molecules. The accompanying uncertainty map for the $T_{\rm D} = 31.3$ K case illustrates that even when the map shows a deep depression there may still exist a substantial amount of material below the sensitivity limit. The field of view in each case is $12.8' \times 12.8'$ and the pixel size is $4''$ (0.16 pc at the assumed 8.4 kpc distance). The tick marks are at intervals of 2 pc. The images were generated by applying `PPMAP` using *Herschel* data in the wavelength range 70–500 $\mu$m.

pect to see some overlying ISM at the Brick location, and the assocated uncertainty map for $T_{\rm D} = 31.3$ K allows for the presence of a significant amount of material there, albeit below the detectability level. Moving to still higher temperatures we find that at $T_{\rm D} = 36.8$ K, a new structure emerges in the interior in the form of a thin hot strip which persists up to $T_{\rm D} = 51.0$ K.

Fig. 2 shows the map of integrated column density obtained by summing the set of differential column densities from all 12 temperature planes of the image cube produced by `PPMAP` using the full data set (*Herschel* plus 1.3 mm). Also shown in this figure is the corresponding map of mean line-of-sight dust temperature obtained from a density-weighted average of the temperatures in the image cube underlying each spatial pixel. Overplotted on both panels are the locations of local density maxima of the hot dust. They correspond to the five strongest maxima in the $T_{\rm D} = 43.3$ K map, and all three maxima at $T_{\rm D} = 51.0$ K. They are listed in Table 1 together with the corresponding values of differential column density and density-weighted mean temperature for the temperature range, 40–55 K, which encompasses both of those temperature bins. The column density and temperature maps in Fig. 2 are consistent with their counterparts presented by Longmore et al. (2012), taking into account the differing values of $\beta$ used and the difference in spatial resolution[2].

Interestingly, the thin hot strip visible in the temperature range 36.8–51.0 K closely overlays the much cooler tadpole feature at 13.9 K. This is illustrated by Fig. 3 which shows a greyscale representation of the differential column density image of 13.9 K material, overplotted with coloured symbols representing the set of all pixels in the 36.8 K, 43.3 K, and 51.0 K images which exceed the $3\sigma$ uncertainty level. This figure shows that, in projection, the structure at all four temperatures is closely coincident, with the higher-temperature material nested within the lower-temperature

[2] Repeating our analysis using the Longmore et al. (2012) value of opacity index, $\beta = 1.75$, gives a total mass of $1.3 \times 10^5\,M_\odot$ as compared to the Longmore et al. value of $1.7 \times 10^5\,M_\odot$. Our peak column density is then a factor of 2.4 higher than the Longmore et al. value and our minimum dust temperature (15.7 K) is about 3 K lower than theirs. Tests with synthetic data (Marsh et al. 2015) indicate that both of these apparent discrepancies can be accounted for by the increased resolution provided by the deconvolution implicit in `PPMAP`. We also find that the key morphological features of our image cube (in particular, the presence of the thin hot strip) are preserved with the alternate choice of $\beta$, although the estimated temperatures are lower—the hot strip then occupies the temperature range 31–43 K rather than 37–51 K.

**Table 1.** Local maxima in the high-temperature dust distribution.

| Peak#[a] | Gal. long. [°] | Gal. lat. [°] | Col. dens.[b] / $10^{20}$ [cm$^{-2}$] | $\overline{T_{\rm D}}$[c] |
|---|---|---|---|---|
| 1 | 0.2512 | 0.0197 | 102 | 43.3 |
| 2 | 0.2523 | 0.0275 | 100 | 43.3 |
| 3 | 0.2557 | 0.0331 | 77 | 43.4 |
| 4 | 0.2601 | 0.0397 | 76 | 44.0 |
| 5 | 0.2623 | 0.0408 | 68 | 43.5 |
| 6 | 0.2557 | 0.0364 | 63 | 48.3 |
| 7 | 0.2612 | 0.0431 | 47 | 49.7 |
| 8 | 0.2568 | 0.0397 | 47 | 50.0 |

[a] Peaks 1–5 and 6–8 are from the 43.3 K and 51.0 K maps, resp.
[b] Total column density in temperature range $T_{\rm D} = 40$–$55$ K.
[c] Density-weighted mean temperature in that same range.

material. This behaviour suggests a cylindrical structure in which the temperature increases outwards.

The mean temperature profile through the "tadpole" feature (averaged over eight lines of sight, each of which corresponds to a pixel located at a local maximum as listed in Table 1 and represented by a red triangle in Fig. 2) is shown in Fig. 4. It is characterised by the presence of two distinct peaks, indicating that the cool and hot material are physically separated at some spatial scale. The same is true of all eight profiles individually. Also shown, for comparison, is the mean temperature profile for the Brick itself, averaged over the region within the boundary defined in Fig. 2.

## 3 DISCUSSION

Much of the dust temperature structure that we have mapped is consistent with external heating of the Brick by the ISRF, as has been discussed in previous work (Lis et al. 2001; Longmore et al. 2012; Clark et al. 2013). In particular, the warm outer sheath manifest as limb brightening at $T_{\rm D} = 31.3$ K is consistent with the predictions of the simulation by Clark et al. (2013). However, we have found that within this cloud, near one edge, is a cool ($T_{\rm D} \sim 14$ K) feature with a tadpole-like geometry, and that a much hotter structure lies within it, at least in 2D line-of-sight projection. Furthermore, there is evidence for temperature stratification such that the hottest material ($T \sim 50$ K) exists within a thin central spine and that the temperature decreases outwards down to the value of $T \sim 14$ K. If the structure were heated externally, we would expect to see the hottest material at the very edge, but Fig. 3 shows that this is not the case, i.e., the temperature actually decreases at the edge. Such behaviour is inconsistent with external heating and it is likely, therefore, that the structure is heated internally. We suggest that it represents a cool filament whose hot cylindrical spine is collapsing and fragmenting to form a line of protostars. We estimate the mass and luminosity of this spine by summing the contributions from material at each of the above three temperatures, and obtain values of $\sim 800\,M_\odot$ and $\sim 6 \times 10^4\,L_\odot$, respectively. The location of peak dust temperature ($\sim 51$ K), in Galactic coordinates, is $[\ell, b] = [0.^\circ2578, 0.^\circ0397]$.

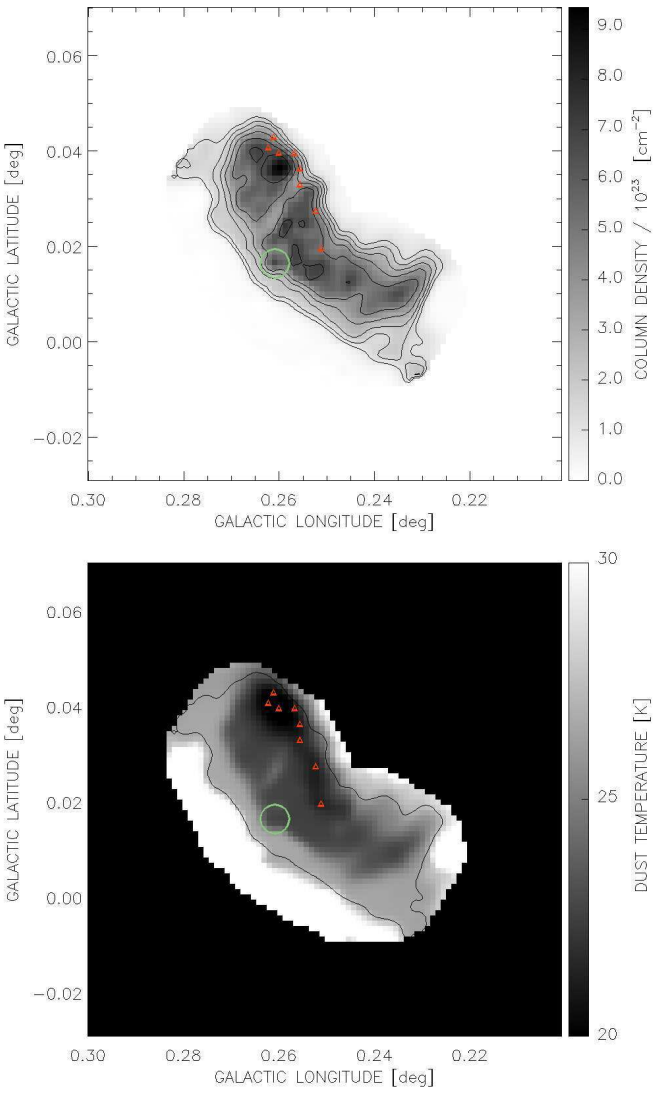


**Figure 2.** Maps of integrated column density and mean temperature. *Upper panel:* Integrated column density, summed over all temperature planes of the image cube of differential column density. Contours are plotted in decreasing intervals of $\sqrt{2}$ from the peak down to a lowest contour level of $1.6 \times 10^{23}$ cm$^{-2}$ which we define as the outer boundary of the Brick. *Lower panel:* Mean (density-weighted) line-of-sight dust temperature. The black curve represents the outer boundary of the Brick as defined above. The field of view of both images is truncated at the bean-shaped outer boundary of the maps published by Johnston et al. (2014), corresponding to the edges of the SMA primary beam in their 6-pointing mosaic. On both panels the red triangles represent the locations of local maxima of hot dust, as listed in Table 1. Also overplotted (green circle) is the location of the water maser reported by Lis et al. (1994).

If indeed the hot spine represents a locus of star formation, then its location near the edge of the cloud is reminiscent, in some ways, of part of the "wishbone" structure of Orion A which has been modelled by Hartmann & Burkert (2007) in terms of nonlinear gravitational acceleration effects. In such models, a star-forming condensation arises at one end of a sheet-like molecular cloud, with density en-

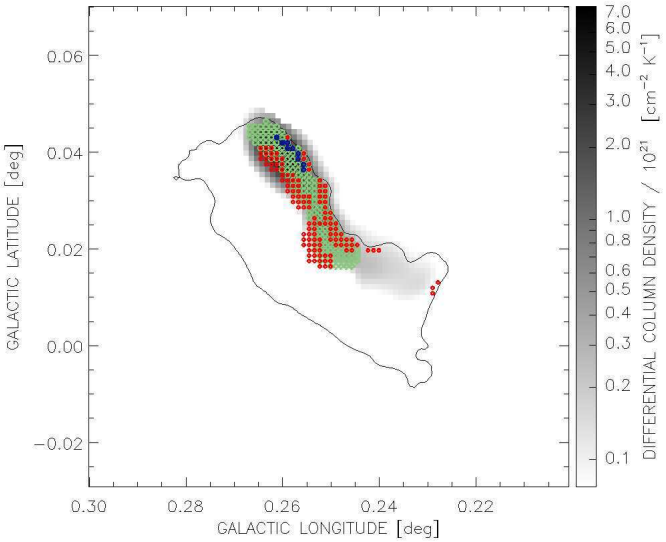


**Figure 3.** The differential column density image at $T = 13.9$ K, shown in greyscale, overlaid by coloured symbols which represent the locations of hot dust at three additional temperatures, namely 36.8 K (red), 43.3 K (green), and 51.0 K (blue). Each plotted symbol (open circle) represents a pixel in which the differential column density exceeds the $3\sigma$ level at the particular temperature. For comparison, the black curve represents the outer boundary of the Brick as defined in Fig. 2.

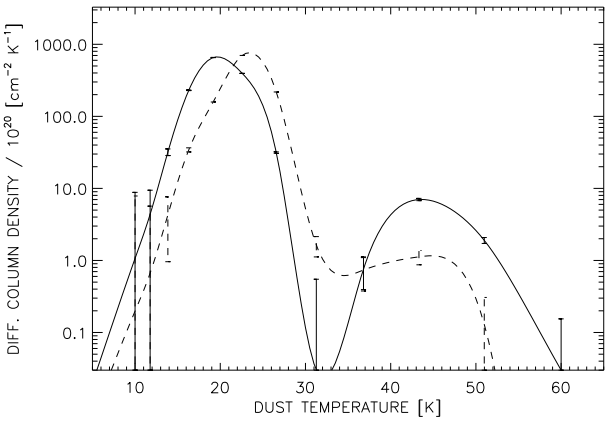


**Figure 4.** Profiles of differential column density as a function of dust temperature. The solid curve represents the average over eight separate lines of sight corresponding to the locations listed in Table 1 and plotted as red triangles in Fig. 2. For comparison, the dashed curve shows the mean profile for the Brick, spatially averaged over the region within the Brick boundary defined in Fig. 2.

hancements extending along the two edges. The fact that the Lis et al. (1994) water maser is also located near an edge, on the opposite side of the Brick, would be consistent with such a scenario. In any event, further observations at high spatial resolution will be necessary to confirm the presence of star formation in the hot spine.

## ACKNOWLEDGMENTS

We thank K. Johnston for a helpful discussion, and also thank the referee for helpful comments. This research is supported by the EU-funded VIALACTEA Network (Ref. FP7-SPACE-607380).

## REFERENCES

Clark, P. C., Glover, S. C. O., Ragan, S. E. et al. 2013, ApJ, 768, L34
Ginsburg, A., Henkel, C., Yipling, A. et al. 2016, A&A, 586, 50
Griffin, M. J., North, C. E., Amaral-Rogers, A. et al. 2013, MNRAS, 434, 992
Güsten, R., Walmsley, C. M., & Pauls, T. 1981, A&A, 103, 197
Hartmann, L. & Burkert, A. 2007, ApJ, 654, 988
Johnston, K. G., Beuther, H., Linz, H. et al. 2014, A&A 568, A56
Kauffmann, J., Pillai, T. & Zhang, Q. 2013, ApJ, 765, L35
Kruijssen, J. M. D., Dale, J. E., & Longmore, S. N. 2015, MNRAS, 447, 1059
Lis, D. C., Menten, K. M., Serabyn, E. & Zylka, R. 1994, ApJ, 423, L39
Lis, D. C., Serabyn, E., Zylka, R., & Li, Y. 2001, ApJ, 550, 761
Longmore, S. N., Rathborne, J., Bastian, N. et al. 2012, ApJ, 746, 117
Longmore, S. N., Kruijssen, J. M. D., Bally, J., et al. 2013, MNRAS, 433, L15
Marsh, K. A., Whitworth, A. P. & Lomax, O., MNRAS, 454, 4282
Mills, E. A. C., & Morris, M. R. 2013, ApJ, 772, 105
Mills, E. A. C., Butterfield, N., Ludovici, D. A. et al. 2015, ApJ, 805, 72
Molinari, S., Swinyard, B., Bally, J., et al. 2010, PASP, 122, 314
Molinari, S., Bally, J., Noriega-Crespo, A., et al. 2011, ApJ, 735, L33
Ossenkopf, V. & Henning, T. 1994, A&A, 291, 943
Pezzuto, S. 2013, HERSCHEL Document Ref.: PICC-CR-TN-044
Pilbratt, G. L., Riedinger, J. R., Passvogel, T., et al. 2010, A&A, 518, L1
Poglitsch, A., Waelkens, C., Geis, N., et al. 2010, A&A, 518, L2
Rathborne, J. M., Longmore, S. N., Jackson, J. M. et al. 2014a, ApJ, 786, 140
Rathborne, J. M., Longmore, S. N., Jackson, J. M. et al. 2014b, ApJ, 795, L25
Rathborne, J. M., Longmore, S. N., Jackson, J. M. et al. 2015, ApJ, 802, 125
Valtchanov, I. 2014, HERSCHEL-DOC-0798, version 2.5, March 24, 2014

This paper has been typeset from a TEX/ LATEX file prepared by the author.